



Trans. Nonferrous Met. Soc. China 34(2024) 2120-2137

Transactions of Nonferrous Metals Society of China

www.tnmsc.cn



Tailoring good combinations between strength and ductility in novel Mg-5Sn-2Al-1Zn alloy via different hot extrusion processes

Feng-jian SHI, Nan-ying PIAO, Ji-heng WANG, Hao-tian TAN, Yu-hang GUO, Fei YANG, Shu-jin CHEN, Sheng LU, Ze-xin WANG

School of Materials Science and Engineering, Jiangsu University of Science and Technology, Zhenjiang 212003, China

Received 7 June 2023; accepted 15 December 2023

Abstract: A novel Mg-5Sn-2Al-1Zn (TAZ521) alloy was prepared. Direct extrusion (DE) and extrusion—shearing (ES) processes were performed on the alloy to improve its strength and ductility. The microstructure evolution, texture evolution, and strengthening mechanisms of as-homogenized and as-extruded alloy were investigated by XRD, SEM, TEM, EBSD, and tensile tests. The results showed that the mechanical properties of the DE-processed alloy were improved. However, the alloy exhibited a bimodal microstructure consisting of coarse grains and fine DRXed grains. After the ES process, the microstructure became more uniform and a good combination of strength and ductility was achieved. The TYS, UTS, and EL were 212 MPa, 303 MPa, and 21.7%, respectively. Grain refinement and pinning effect by Mg₂Sn precipitates play an important role in the enhancement of strength. Additionally, the improvement of ductility is attributed to the weak basal fiber texture and the activation of non-basal slip.

Key words: Mg-Sn-Al-Zn alloys; extrusion-shearing; grain refinement; mechanical properties; texture evolution

1 Introduction

Magnesium (Mg) alloys have great potential in automotive, aerospace, and communication fields owing to their advantages of low density, high specific stiffness, and extraordinary environmental protection performance [1–3]. However, the applications of Mg alloys are extremely restricted due to their high yield anisotropy and low ductility [4]. Therefore, it is essential to develop magnesium alloys with enhanced mechanical properties for industrial applications.

Commercial Mg alloys, such as AZ31 and ZK60, have been widely used nowadays. Although the Mg–Zn alloy system shows potential for improving the mechanical properties through age hardening, the best properties will not be achieved if grain growth is minimized after solution

treatment [5]. As for the Mg-Al alloy system, aluminum is well-known for its great solid-solution strengthening ability, but the Mg-Al alloys still unacceptable strength for large-scale applications [5]. Mg-Sn based alloy, a kind of casting alloy with low cost, and superior extrudability, has attracted increasing attention these years as the Mg₂Sn phase shows a compromising improvement on the mechanical properties of Mg alloys [6]. Besides, the Mg₂Sn phase with $Fm \overline{3}m$ structure (a=0.676 nm) shows high-temperature stability, which leads to the great potential of the Mg-Sn based alloy with higher temperature creep resistance [7]. LUO et al [8] reported that Mg-3Sn-5Zn-Al alloys showed great mechanical properties with values of the ultimate tensile strength (UTS) and elongation (EL) of 340 MPa and 20.1%, respectively. The activity of non-basal slip, finer microstructure, and texture

with a relatively lower density were the main factors for the great mechanical properties of Mg-Sn based alloys. ZHANG et al [9] investigated the effect of extrusion ratio on the properties of TZX621 alloys. They found that the extruded TZX621 alloys exhibited a finer microstructure when the extrusion ratio increased from 6 to 16, and the YS and UTS were improved by 36.0% and 17.7%, respectively. However, the elongation only exhibited a slight increase from 15.6% to 18.1%. The reduction of unDRXed grains and average grain size were believed to be the reasons for the improvement in mechanical properties. According to related literature, Mg₂Sn precipitates with high melting points could be formed in the Mg matrix, which will contribute to precipitate strengthening. On the other hand, Sn is effective in decreasing the stacking fault energy of Mg alloys, blocking the interact slips of dislocations, and promoting the activation of non-basal slip systems when the content of Sn elements reaches a critical point [10]. However, most previous work is focused on the strengthening effect of Mg₂Sn precipitate, while the plasticity seems to be neglected during deformation.

As one of the most promising severe plastic deformation (SPD) methods, equal channel angular pressing (ECAP) has been widely used to improve the mechanical properties of Mg alloys by grain refinement. According to the Hall-Petch relationship, grain refinement can contribute to the increase in strength [11]. Additionally, grain refinement can contribute to the decrease of the critical resolved shear stress (CRSS) of non-basal slips, so the activation of basal slips is weakened and the ductility is improved [12]. Combining the conventional direct extrusion (DE) and the shearing process of ECAP deformation, the extrusionshearing (ES) process has been suggested to further optimize the strength of Mg alloys without sacrificing ductility. In order to improve the mechanical properties, the extrusion-shearing process was applied to a novel Mg-5Sn-2Al-1Zn (TAZ521) alloy in this work. Afterward, the microstructure characteristics, texture evolution, and mechanical properties were systematically discussed in detail. The proposed deformation in this work provides new insights for improving the strength of Mg-Sn based alloys without sacrificing ductility and manufacturing methods more efficiently.

2 Experimental

2.1 Sample preparation

The commercially pure Mg, Sn, Al, and Zn blocks (with a purity of 99.99 wt.%) were used in this study to prepare Mg-5Sn-2Al-1Zn (TAZ521) alloys. The materials were melted in an electrical resistance furnace under the protective atmosphere of SF₆ and CO₂ mixed gas with a mixing volume ratio of 1: 99. The molten alloy was kept at 750 °C for 20 min and then poured into a previously preheated stainless steel mold (d80 mm × 220 mm) with a preheating temperature of 300 °C. The homogenization treatment was then carried out at 425 °C for 24 h followed by air cooling to eliminate defects and element segregation in as-cast alloys. The as-homogenized TAZ521 ingot was machined into cylinders with a size of $d20 \text{ mm} \times 40 \text{ mm}$ for extrusion. These rods were preheated at 250 °C for 15 min before hot extrusion. Hot extrusion with an extrusion rate of 2 mm/s was carried out at 250 °C and the extrusion ratio is 4:1. The extruded rods were quenched in water immediately after extrusion. The detailed illustrations of different processes are shown in Fig. 1.

2.2 Microstructure characterization

Figure 1(d) shows the observation position of the specimen. All the samples were ground with SiC sandpaper from 600 grit to 2000 grit and then were etched with the mixed solution (2 g picric acid, 4 mL acetic acid, 4 mL H₂O, and 32 mL ethanol) for 10 s. Phase constitution and macrotexture of the alloys were identified by using an X-ray diffractometer (XRD, D8 advance) with Cu K_{α} radiation. The diffraction angles ranged from 20° to 90° and the scanning speed was 1 (°)/min. The collected data were analyzed by Jade 6.5 software. Macrotexture analyses were performed on the basal plane (0001), prismatic plane ($10\overline{10}$), and pyramidal plane $(10\overline{1}1)$. The measurements were conducted on the planes parallel to the extrusion direction (ED). The microstructural characterization, morphologies, and element compositions of the TAZ521 alloys were analyzed using an optical microscope (OM, VHX-900), scanning electron microscopy (SEM, ZEISS Merlin Compact SEM) equipped with an energy dispersive spectrometer (EDS), transmission electron microscopy (TEM,

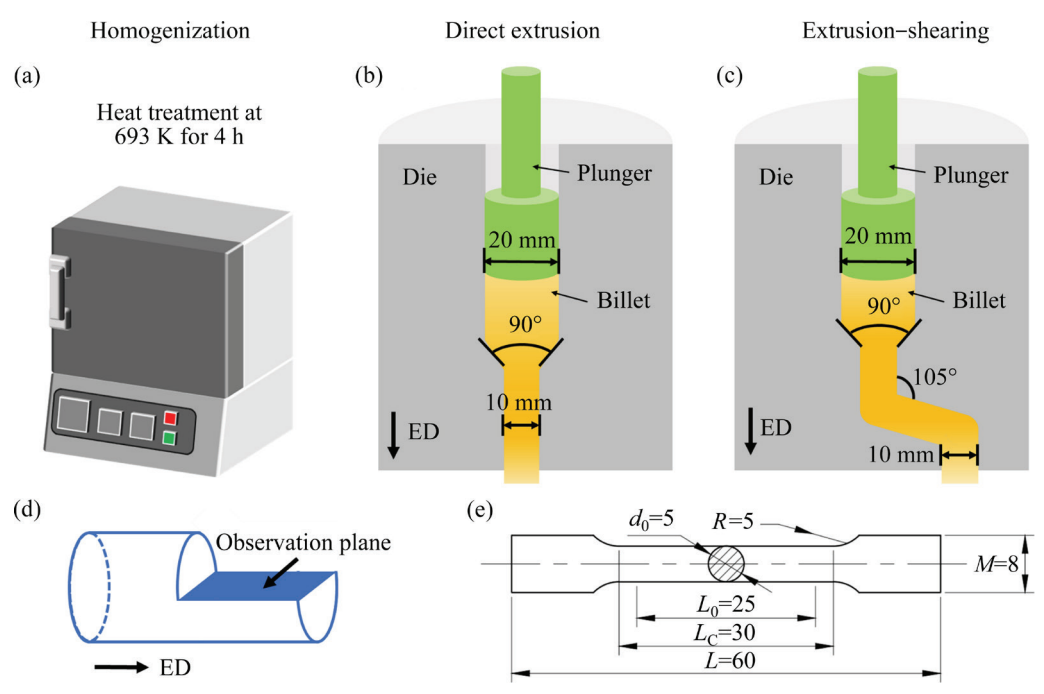


Fig. 1 Schematic illustrations of homogenization (a), direct extrusion (b), and extrusion—shearing (c) processes, and schematic diagrams of observation position of sample (d) and tensile specimen (unit: mm) (e)

JEOL–2100F) and electron backscatter diffraction (EBSD). The samples for the EBSD test were ground with 3000 grit sandpapers and then polished in the AC II solution for about 100 s at $-20\,^{\circ}$ C with a working voltage of 20 V. The scanning step lengths for the as-homogenized, DE-processed, and ES-processed samples are 3, 0.4, and 0.4 μ m, respectively. The EBSD data were analyzed by the HKL Channel 5 software. The samples were mechanically ground to about 40 μ m and punched into small discs with a diameter of 3 mm for TEM testing. These discs were then ion-thinned via Gatan 691 with both high and low gun angles of 4° and a voltage of 3.5 keV.

2.3 Mechanical testing

As shown in Fig. 1(e), the dog-bone-shaped specimens with a gage length of $d5 \text{ mm} \times 25 \text{ mm}$ were used for tensile testing with a SANS universal testing machine at a constant strain rate of $1.0\times10^{-3}\,\text{s}^{-1}$. The tensile test was conducted at room temperature and the loading axis corresponded to the extrusion direction.

3 Results

3.1 Microstructures

Figure 2 exhibits the optical micrographs of

the TAZ521 alloys. The microstructures consist of α -Mg matrix and precipitates located at the grain boundaries and inside the grains. The ashomogenized sample shows equiaxed grains, with size of 50–90 μ m. The sample processed by DE presents a significant microstructure with elongated grains surrounded by small equiaxed grains (white circles in Figs. 2(c, d)). After the ES process, the sample becomes more homogeneous and the distribution of the precipitates becomes finer and more dispersive. Compared to the DE process, the grain size is further refined through the ES process.

To further analyze the composition of the precipitates of the TAZ521 alloy, XRD and SEM-EDS analyses were performed. The XRD patterns (Fig. 3) reveal that the main compositions of the TAZ521 alloy are α-Mg matrix and Mg₂Sn. Besides, the equilibrium phase diagram confirmed that the composition of the microstructure is a two-phase structure (α-Mg + Mg₂Sn) according to previous studies [13,14]. The peak intensity of the basal texture (002) shows an obvious increase after DE, indicating the formation of (002) fiber texture. The intensity of (100) increases, while the intensity of (002) has a slight decrease during ES, which may lead to the weakening of the basal texture.

Figures 4(a-c) show the SEM micrographs of the TAZ521 alloys performed with different

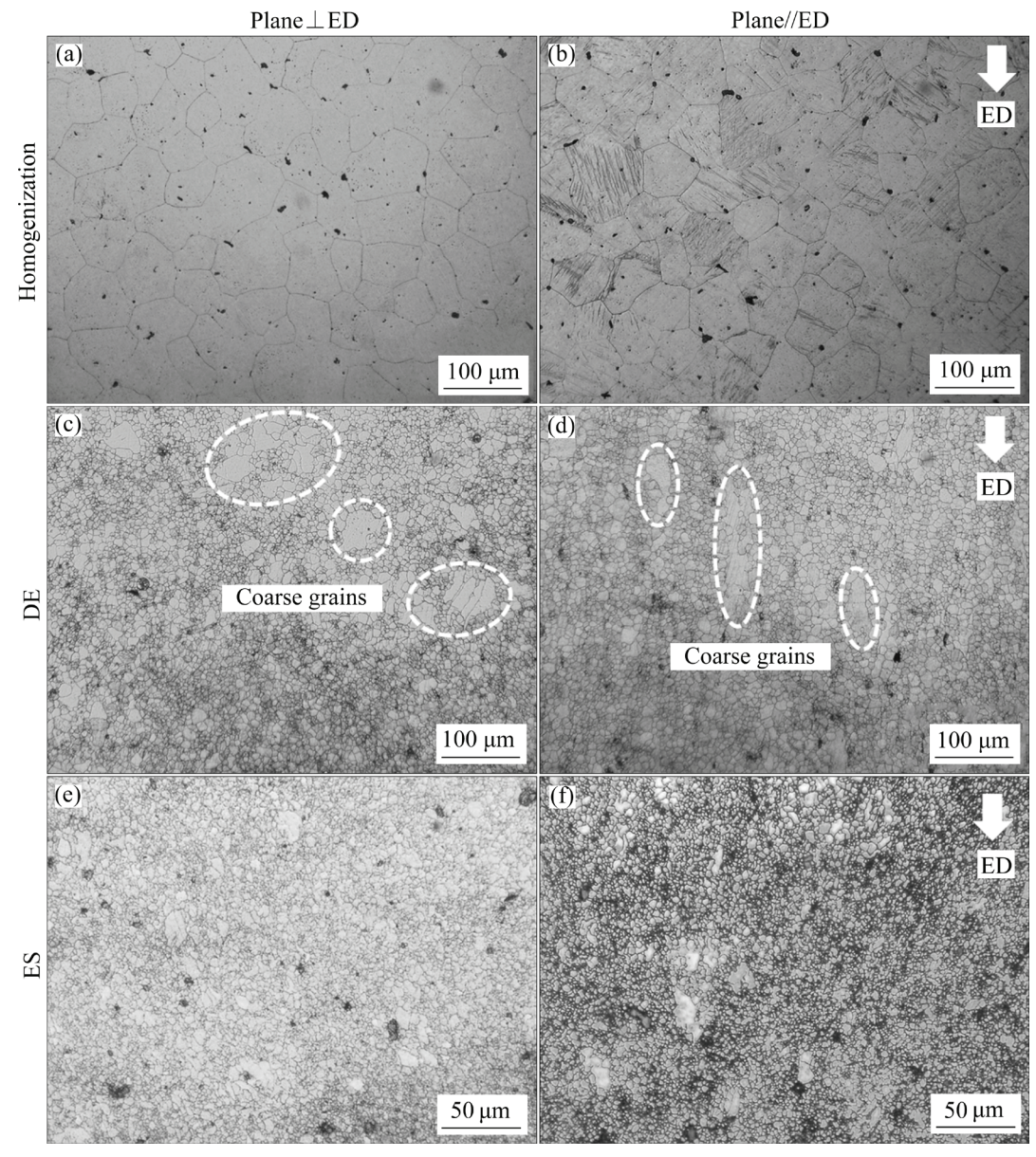


Fig. 2 Optical micrographic images of TAZ521 alloys with different processes: (a, b) Homogenization; (c, d) DE; (e, f) ES

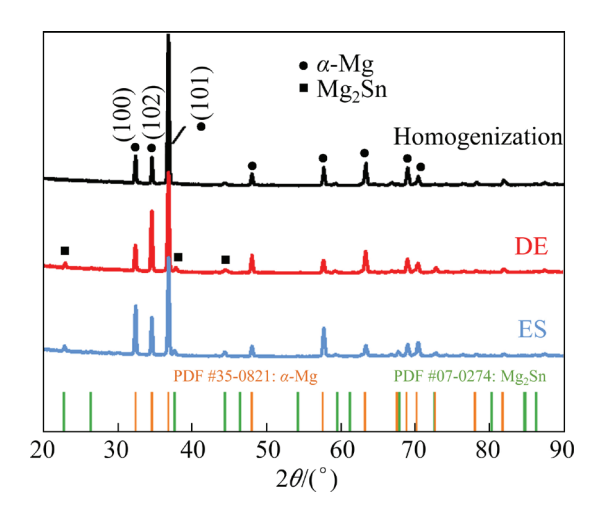


Fig. 3 XRD patterns of TAZ521 alloys

irregular and processes. Several spherical precipitates (marked by yellow arrows) can be observed in Fig. 4(c). According to the EDS results (Table 1), the atomic ratio of Mg and Sn is about 2:1; therefore, the spherical undissolved precipitates can be identified as Mg₂Sn phases, which is consistent with the XRD results. Since the Mg₂Sn phase has a high melting point of 1043 K [15], it is reasonable for a few Mg2Sn phases to remain in the alloy after hot treatment, therefore leading to differences in the microstructures and tensile properties. These precipitates are broken into micro-sized particles after extrusion. These fine particles can provide nucleation sites for dynamic

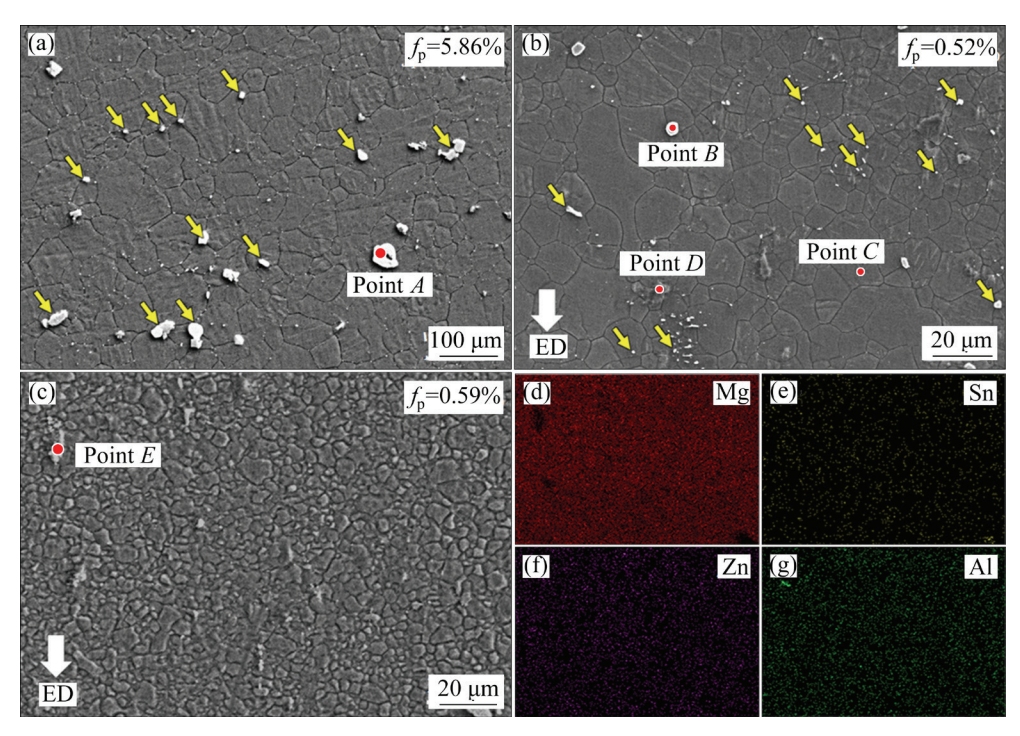


Fig. 4 SEM images of as-homogenized (a), DE-processed (b), and ES-processed (c) alloys and corresponding EDS mappings (d-g) of ES-processed sample (f_p -Volume fraction of precipitates)

Table 1 Corresponding EDS results of TAZ521 alloys in Fig. 4

Point -	Element content/at.%				Dl
	Mg	Sn	Al	Zn	Phase
A	69.89	28.48	1.21	0.42	Mg_2Sn
B	72.31	26.81	0.65	0.23	Mg_2Sn
C	97.52	1.34	0.89	0.25	α-Mg
D	85.53	13.53	0.75	0.19	Mg_2Sn
E	88.63	11.17	0.12	0.08	Mg_2Sn

recrystallized (DRXed) grains through particlesstimulated nucleation (PSN) mechanism [16]. It can be learned from the EDS mappings of the ES-processed sample that most elements are dissolved into the matrix. The fractions of these precipitates are measured to be about 5.86%, 0.52%, and 0.59%, respectively. The low fraction of precipitates in the ES-processed sample may not make much contribution to strengthening.

Figure 5 shows the TEM morphology of the TAZ521 alloys. It can be observed from Fig. 5(a) that some precipitates are located at the grain boundary and the average size of the large bulk precipitate is about 1 μ m. After the DE and ES processes, nano-scale particles are precipitated along the grain boundaries, which can inhibit grain

growth and thus contribute to the hardening effects. Besides, the grains contain numerous residual dislocations to form dislocation entanglement, as depicted in Figs. 5(b, c). The thermal stress and deformation energy can be generated during extrusion. Therefore, there is an increase in the dislocation density, which can activate either basal slip or non-basal slip. The nano-scale precipitates can hinder the dislocation movement and the grains are separated into small regions and sub-grains are eventually formed, thereby contributing to the improvement of the strength [17]. The bright field TEM image viewed under $[11\bar{2}0]_{a-Mg}$ zone axis is shown in Fig. 5(d) and the α -Mg matrix can be indexed by the corresponding selected area electron diffraction (SAED) pattern. According to the SAED pattern shown in Fig. 5(e), the nanoscale precipitates can be identified as face-centered cubic (FCC) Mg₂Sn phases. The HRTEM results illustrate the orientation relationship between α -Mg matrix and Mg₂Sn precipitate: $[11\overline{2}0]_{\alpha\text{-Mg}}/[\overline{1}22]_{\text{Mg}_2\text{Sn}}$.

3.2 Macro-texture evolutions

Figure 6 shows the macro-texture of TAZ521 alloys with different processes. As can be seen, the pole density points of (0001) are distributed mainly along the edge of the polar diagram and the texture

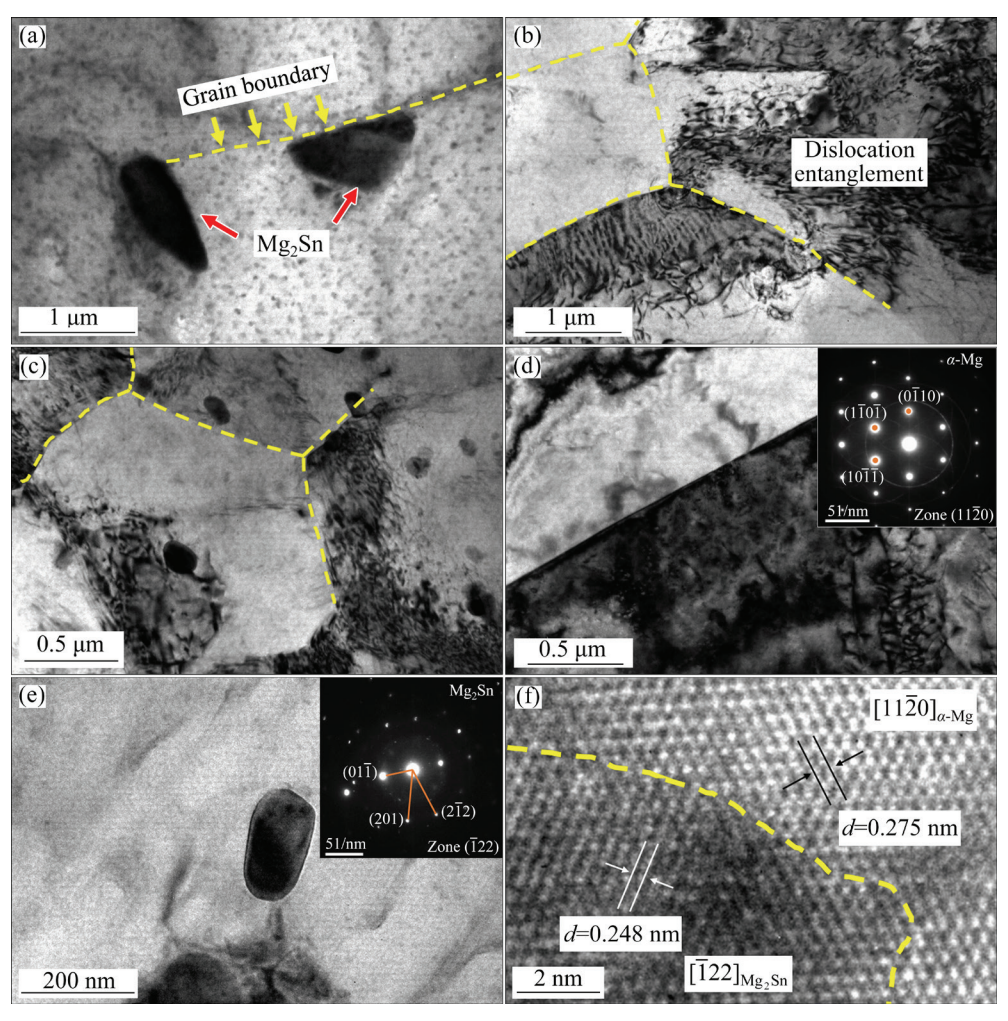


Fig. 5 TEM morphology showing second phase of as-homogenized TAZ521 alloy (a); Two-beam bright-field TEM images of dislocation tangling with high density in grains of DE-processed sample (b) and ES-processed sample (c); Bright field TEM image and corresponding SAED pattern (inset) of DE-processed sample under [1120]_{α-Mg} zone axis (d); TEM image of precipitate in ES-processed TAZ521 alloy and corresponding SAED pattern (inset) (e); HRTEM micrograph of Sn-rich precipitate (f)

density of the (0001) plane increases slightly from 4.55 to 5.07, inferring that the TAZ521 alloys show a predominant basal texture (0001)//ED, which is consistent with the XRD results. The intensity area of $(10\overline{1}0)$ pole figures are mostly distributed at the edge of ED, which means that the alloy shows a preferred orientation with (1010)//TD. The maximum intensity of $(10\overline{1}0)$ pole figures increases from 2.51 to 3.51, which indicates that most grains exhibit a strong basal texture after the DE process. During the ES process, the pole density area is still distributed at the edge and a slight decrease in intensity can be found in the $(10\overline{1}0)$ pole figure. This could be attributed to the shear deformation of the ES process. Furthermore, the distribution of pole density points of both $(10\overline{1}1)$ and $(10\overline{1}0)$ pole figures gradually become scattered, which is mainly caused by the rotation of grains.

3.3 EBSD results

Figure 7 shows the grain orientation maps, grain boundary maps, and distributions of grain size of the TAZ521 alloy with different processes. Different colors in the grain orientation maps represent different grain orientations. As can be seen from Fig. 7(a), the as-homogenized sample exhibits random grain orientations and the average grain size is about 49.7 μm. After the DE process, some grains tend to present red and purple colors, which indicates that the (0001) planes of the grains are parallel to ED. Besides, It can also be seen from

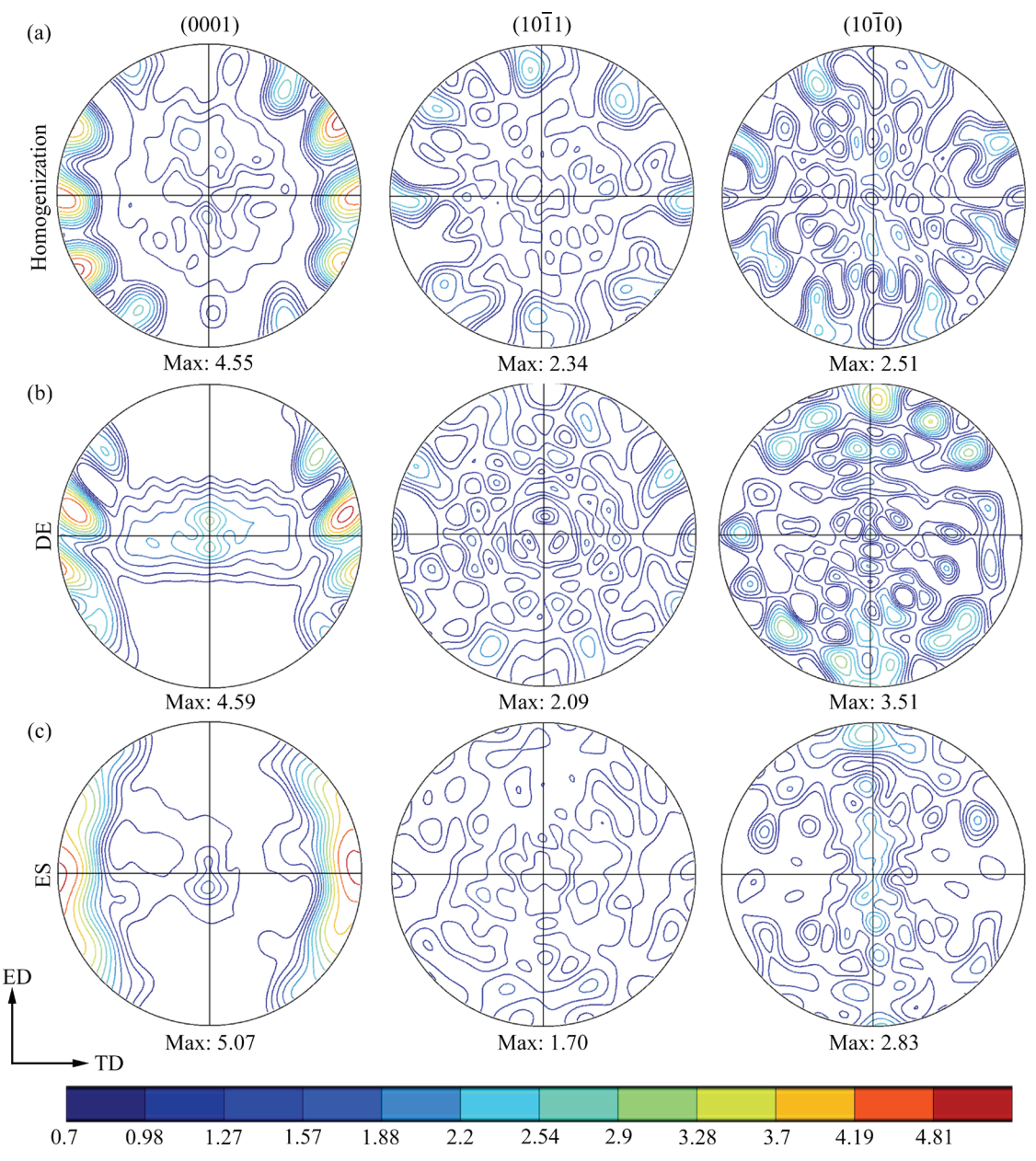


Fig. 6 Macro-texture evolution of TAZ521 alloys after different processes: (a) Homogenization; (b) DE; (c) ES (TD is the transverse direction)

the grain orientation map that some unbroken grains are surrounded by a large number of fine equiaxed grains. The grain size of the DE-processed sample decreases significantly, with an average grain size of about 4.8 μ m. Different from the DE-processed sample, the majority of the grains show blue and green colors after the ES process, indicating that the (10 $\overline{10}$) and ($\overline{1210}$) planes of the grains are parallel to ED. Therefore, it can be deduced that the grain orientations are changed through the ES process. The grains are greatly refined and the sample exhibits a more uniform microstructure. The average grain size decreases slightly due to the

increasing accumulative strain from the DE to ES process, with an average grain size of about $2.8 \mu m$.

To further understand the evolution of the microstructure, the grain boundary maps are also presented, where the blue lines represent the low-angle grain boundaries (LAGBs, $2^{\circ} < \theta < 15^{\circ}$) and the red lines represent the high-angle grain boundaries (HAGBs, $\theta > 15^{\circ}$). As shown in Figs. 7(b, e, h), the fraction of LAGBs is estimated to be 18.9%, 7.2%, and 7.6% for the as-homogenized, DE, and ES-processed samples, respectively. It can be observed that a large number of LAGBs are concentrated in the grains and then divide the non-dynamically

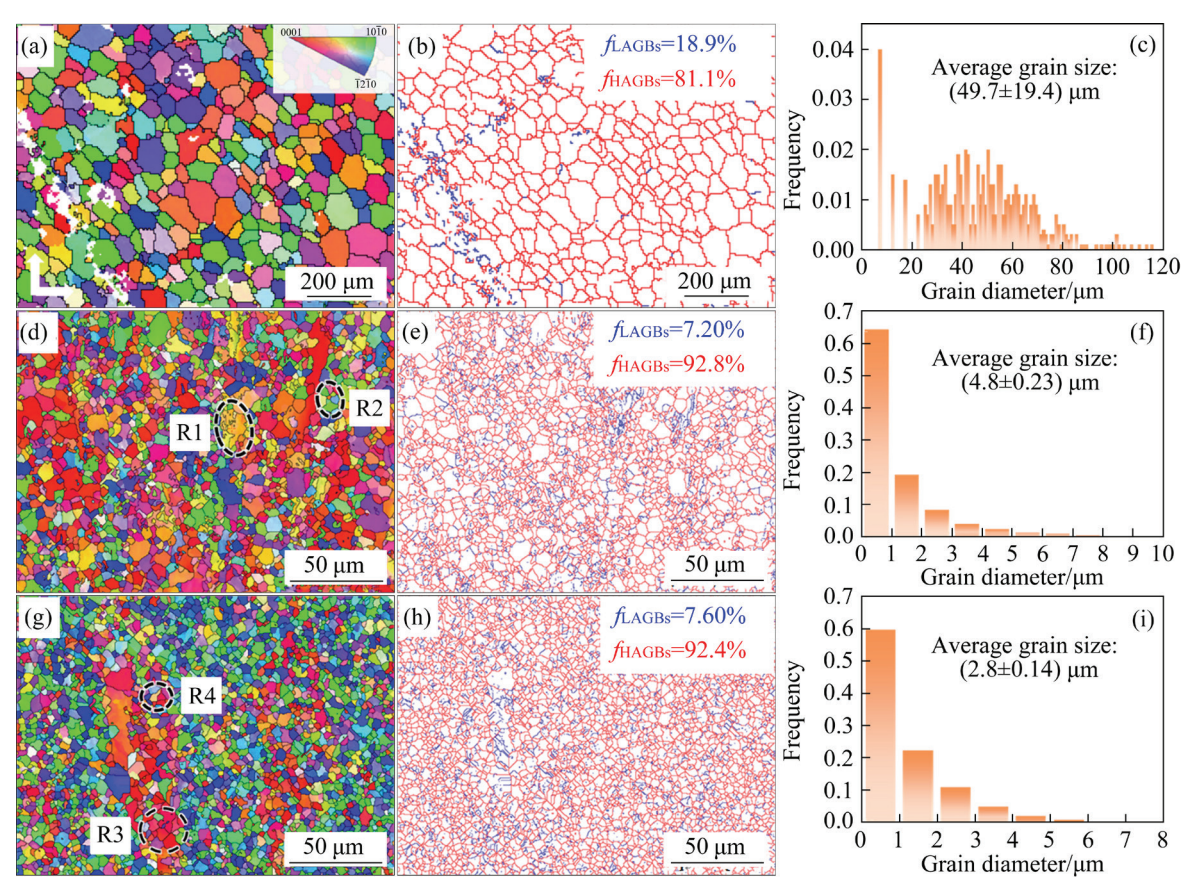


Fig. 7 EBSD results of TAZ521 alloys after homogenization (a-c), DE (d-f) and ES processes (g-i): (a, d, g) Grain orientation maps; (b, e, h) Corresponding grain boundary maps; (c, f, i) Distribution histograms of grain size

recrystallized grains into small sub-grains. After the DE process, the new DRXed grains gradually grow by absorbing high-density dislocations, transforming LAGBs into HAGBs. As accumulative strain increases during the ES process, the dislocation migration ability increases, resulting in the transformation of LAGBs into HAGBs by the driving force of grain boundary energy. Therefore, the volume fraction of HAGBs is similar in the DE-processed and the ES-processed samples, which is consistent with the results of references [15,18].

The kernel average misorientation (KAM) maps and distributions of the corresponding KAM value of the TAZ521 alloys are shown in Fig. 8. Higher KAM value indicates a higher dislocation density and higher plastic deformation degree. As shown in Fig. 8(a), the dislocations are concentrated around the grain boundaries at first. As the accumulative strain reaches a certain extent, the nucleation of dynamic recrystallization is promoted and the newly generated grains gradually grow by consuming the accumulated internal strain energy [19]. Therefore, the geometrically necessary

dislocation (GND) density is brought out to calculate the residual dislocation density. The GND density has a linear relation with the average KAM value and can be calculated by [20]

$$\rho_{\text{GND}} = 2\theta/(\mu b) \tag{1}$$

where $\rho_{\rm GND}$ is the GND density; θ represents the average KAM value; μ is the step size (3 and 0.4 μ m); b is the magnitude of Burgers vector (0.32 nm). Any local misorientation angles less than 5° are counted to calculate the average KAM value. The calculated GND densities of the ashomogenized, DE, and ES-processed alloys are about 0.33×10^{13} , 0.41×10^{14} and 0.46×10^{14} m⁻², respectively. The ES-processed sample shows a higher dislocation density, which means that more stress is needed to migrate the dislocations to their neighbor grains, leading to an enhancement in the strength.

3.4 Mechanical properties

Figure 9(a) displays the tensile stress-strain curves at room temperature of the as-homogenized,

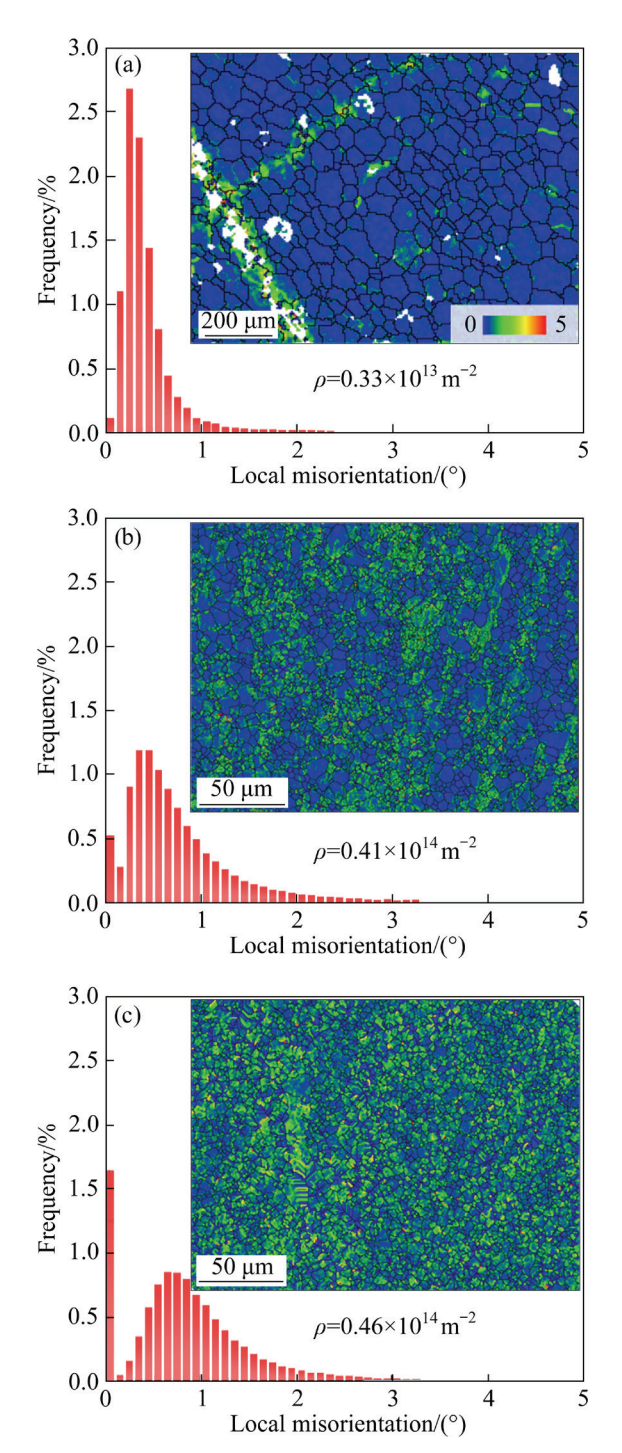


Fig. 8 Kernel average misorientation (KAM) maps and distributions of KAM value of TAZ521 alloys with different processes: (a) Homogenization; (b) DE; (c) ES

DE and ES-processed samples. Detailed statistics about the tensile yield strength (TYS), ultimate yield strength (UYS), and elongation (EL) are summarized in Table 2. The TYS, UYS, and EL of the as-homogenized sample at room temperature are 84 MPa, 142 MPa, and 6.1%, respectively. After the DE process, TYS and UYS of TAZ521 alloy

reach 165 MPa and 264 MPa, respectively, which are increased by 96.4% and 85.9% compared to those of the as-homogenized sample. Besides, the elongation is 15.9% and increased by 160.7%. The TYS and UYS of the ES-processed sample reach 212 MPa and 303 MPa, respectively. At the same time, the elongation increases to 21.7%, by 255.7% compared to that of the as-homogenized sample, indicating that the ES process is an effective method to enhance the strength and ductility of TAZ521 alloys.

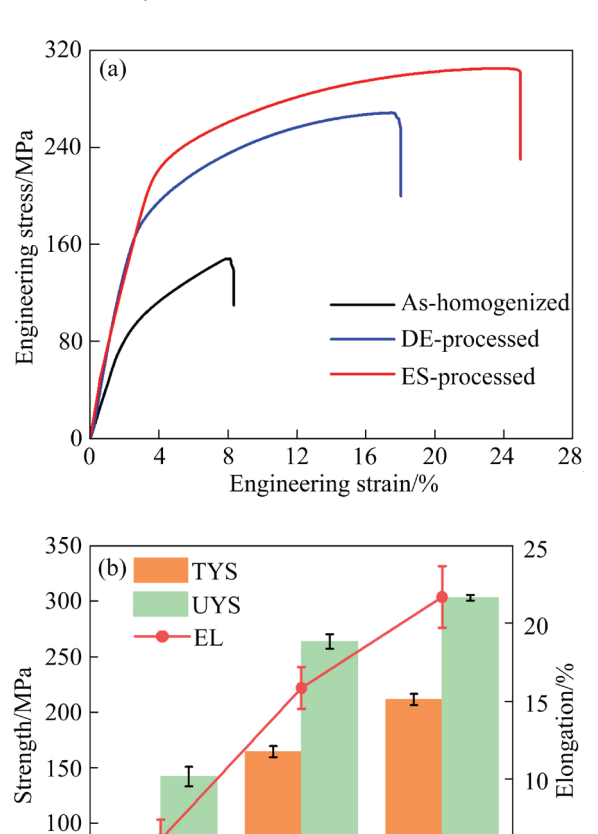


Fig. 9 Engineering stress—strain curves of ashomogenized, DE-processed, and ES-processed samples at room temperature (a); Comparison of mechanical properties after different processes (b)

As-homogenized DE-processed ES-processed

Sample

50

5

Table 2 Tensile mechanical properties of TAZ521 alloy after different processes

Process	TYS/MPa	UYS/MPa	EL/%
Homogenization	84±2.7	142 ± 8.8	6.1±1.3
DE	165 ± 5.0	264 ± 6.7	15.9 ± 1.3
ES	212±5.0	303±2.6	21.7±2.0

The SEM morphologies of the tensile fracture at room temperature are shown in Fig. 10. The fracture characteristics of the as-homogenized sample are cleavage planes (black arrows), which are the typical features of brittle fracture [21]. As shown in Figs. 10(b, c), the morphologies of the DE-processed sample contain dimples (red arrows) and some large-sized precipitates (white arrows) located at the bottom of the dimples. Few smooth facets (yellow arrows) can be observed, showing brittle fracture features. The fracture morphologies indicate poor mechanical properties, which are consistent with the tensile results. The fracture morphologies of the ES-processed alloys exhibit fine and uniform dimples and tear ridges (blue arrows), which are considered ductile fractures. It is suggested that extra energy is absorbed during the formation of these fine dimples, therefore leading to the improvement of ductility. Moreover, it can be observed that precipitates are broken into smaller blocks compared to those in the DE-processed sample. These dispersedly distributed particles make a great contribution to the enhancement of strength.

4 Discussion

4.1 Microstructure evolutions

Figure 11 shows the CDRX behavior and the corresponding effects on the grain orientation evolution in R1 and R3 selected in Figs. 7(d, g), respectively. As shown in Figs. 11(a, d), a large number of LAGBs can be seen in parent grains and these LAGBs divide the parent grains into several sub-grains. Moreover, the parent grains are surrounded by some fine dynamically recrystallized grains along the grain boundaries or inside the parent grains. Figures 11(c, f) show the curves of

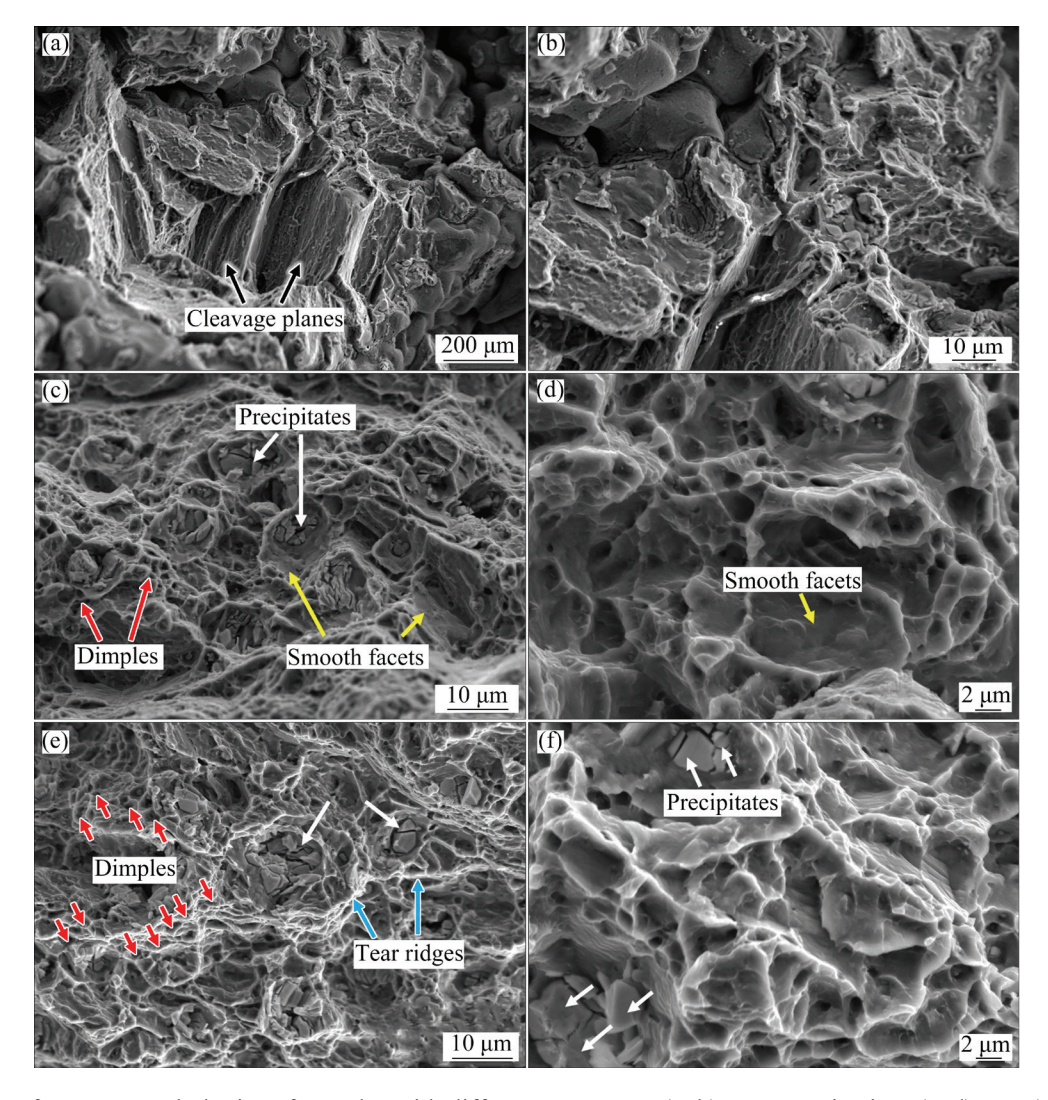


Fig. 10 SEM fracture morphologies of samples with different processes: (a, b) Homogenization; (c, d) DE; (e, f) ES

misorientation degrees of the black arrows AB and CD presented in Figs. 11(a, d). It can be found that the parent grains have a large orientation gradient, which indicates that there are a great number of dislocations in these parent grains. It can be learned from the literature [22] that the cumulative strain during deformation may contribute to the dislocations in the grains, which can rearrange or merge to generate sub-grains and gradually absorb more dislocations to form DRXed grains. The corresponding (0001) pole figures are presented in Figs. 11(b, e). The grain orientations of sub-grains are very close to the parent grains and the orientation of the newly DRXed grains exhibits a more scattered distribution. In general, these grains all present a preferred orientation.

Figure 12 presents the discontinuous dynamic recrystallization (DDRX) behavior and the corresponding grain orientation distribution in R2 and R4 selected in Figs. 7(d, g), respectively. According to SITDIKOV and KAIBYSHEV [23], the grain boundary dislocation provides the accommodation of plastic deformation and these dislocations are mainly non-basal systems. The interaction of these basal dislocations yields the formation of sub-grain boundaries, which cut off

the protrusion from the grain body, and then the misorientation of sub-grain boundaries increases through gathering dislocations, finally leading to the formation of HAGBs [23]. Furthermore, the non-basal systems are easier to be activated due to the grain-boundary compatibility stress. Accordingly, the grain refinement and the activity of non-basal slip systems contribute to the DDRX behavior. As shown in Figs. 12(b, c) and 12(e, f), the pole figures and inverse pole figures (IPF) show that the newly DRXed grains exhibit different orientations compared to the parent grains, indicating that the DDRX mechanism contributes to the randomly distributed grain orientation.

Figure 13 presents the distribution mappings of the TAZ521 alloys with different processes and corresponding statistical frequencies of different grain regions, where the blue area represents recrystallized grains, the yellow area represents sub-grains, and the red area represents deformed grains. Figure 13(b) shows that the percentage of DRXed grains is 25%, indicating few grains undergo dynamic recrystallization during the DE process. It is suggested that more nucleation sites are provided for DRXed grains by accumulating high-density dislocations during deformation,

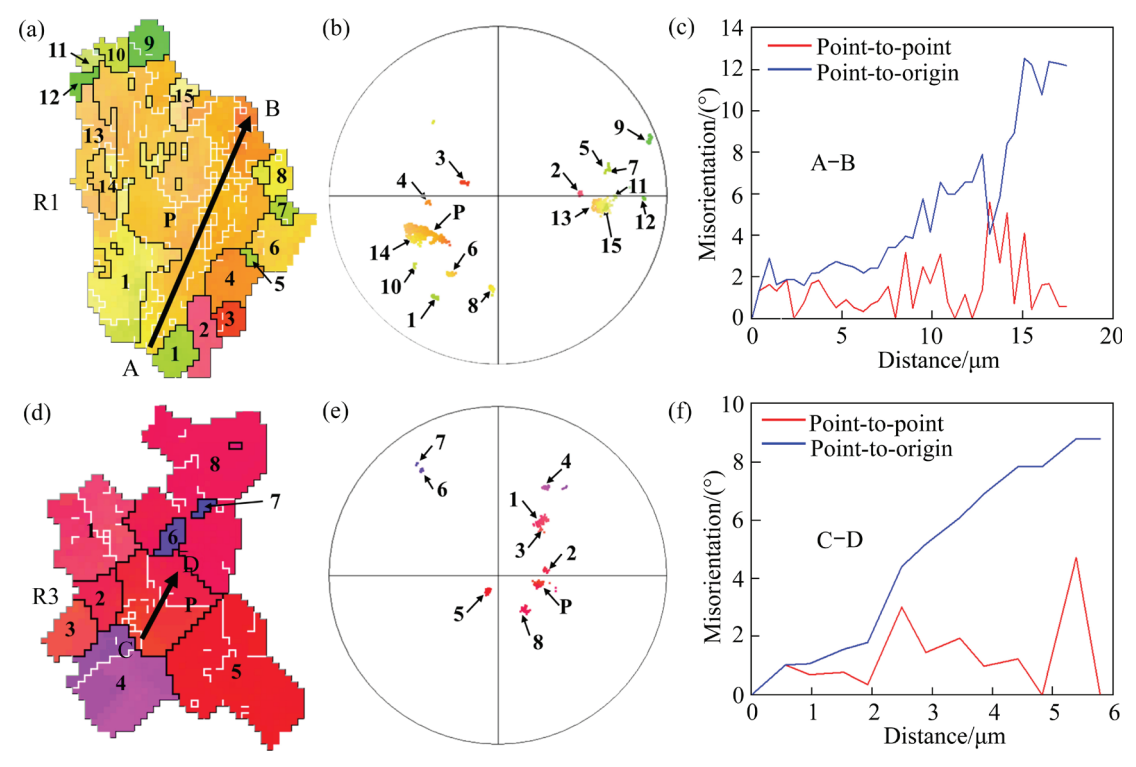


Fig. 11 CDRX behavior and corresponding effects on grain orientation evolution in R1 (a-c) and R3 (d-f) selected in Fig. 7: (a, d) Grain orientation maps; (b, e) (0001) pole figures; (c, f) Curves of misorientation degrees of black arrows AB and CD

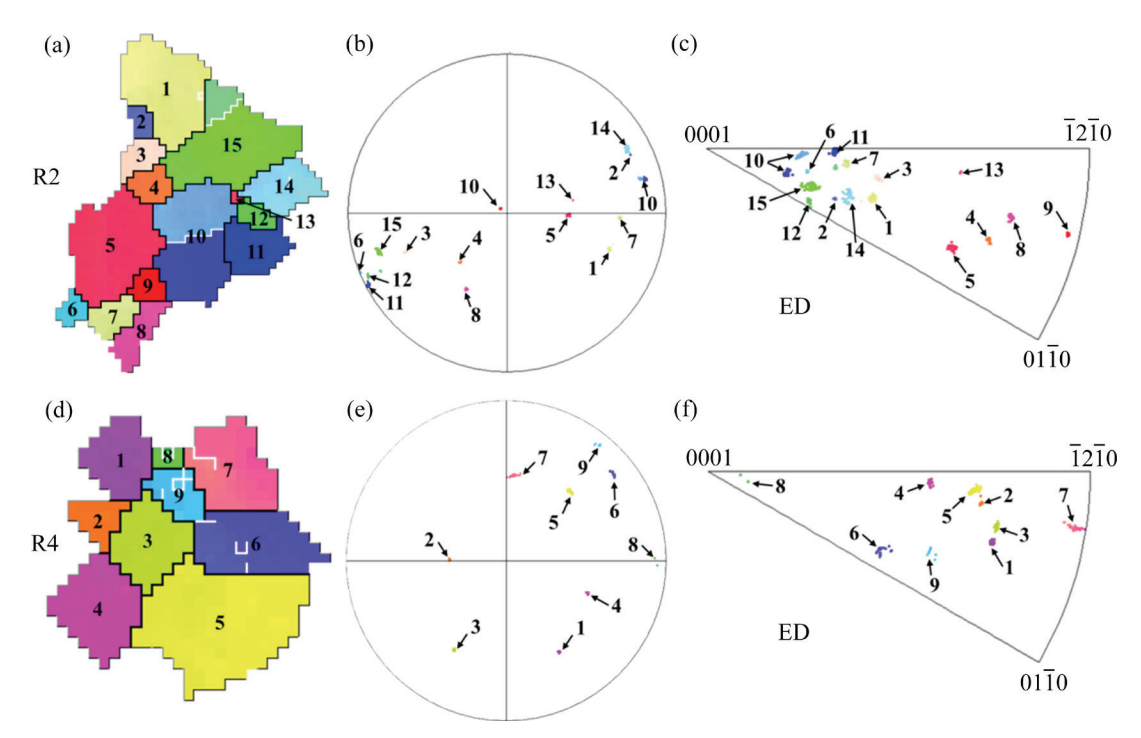


Fig. 12 DDRX behavior and corresponding grain orientation distribution in R2 (a-c) and R4 (d-f) selected in Fig. 7: (a, d) Grain orientation maps; (b, e) (0001) pole figures; (c, f) Inverse pole figures (IPFs)

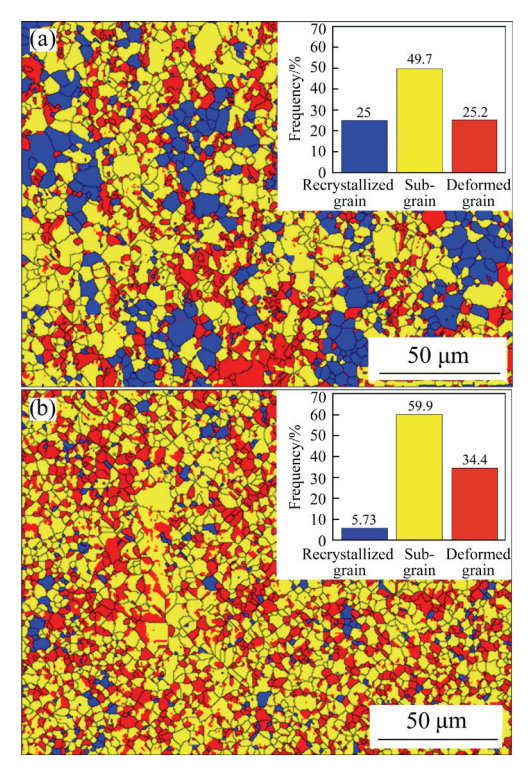


Fig. 13 Distribution mappings of TAZ521 alloys and corresponding statistical frequencies of different grain regions: (a) DE-processed sample; (b) ES-processed sample

hence promoting dynamic recrystallization grain refinement [24]. The sub-grains show a relatively higher fraction, which is mainly due to the high dislocation density. About 25% of grains have insufficient internal storage energy, therefore exhibiting deformed grains. After the ES process, the majority of grains remain sub-grains with a percentage of 59.9%. It could not be neglected to find that the proportion of DRXed grains decreases to 5.73%. According to Fig. 8(c), few dislocations are formed after two passes of shearing deformation. It can be deduced that these uniformly distributed dislocations in the grains lead to an increasing number of sub-grains, which is consistent with the results of GUO et al [15]. Moreover, the small precipitates provide more nucleation sites for the dynamic recrystallizations and DRX grain refinement through accumulating high-density dislocations during deformation. It is pointed out that nano-sized secondary phase particles (<1 µm) may lead to the grain-boundary pinning effect, hence hindering recrystallization nucleation and grain growth [24]. In this work, both the dynamic precipitation of Mg₂Sn and nano-sized secondary precipitates hinder the DRX through the grainboundary pinning effect. Therefore, the volume fraction of the recrystallized grains decreases.

4.2 Texture evolutions

Figure 14 shows the (0001) pole figures of the TAZ521 alloys. It can be seen that the basal pole

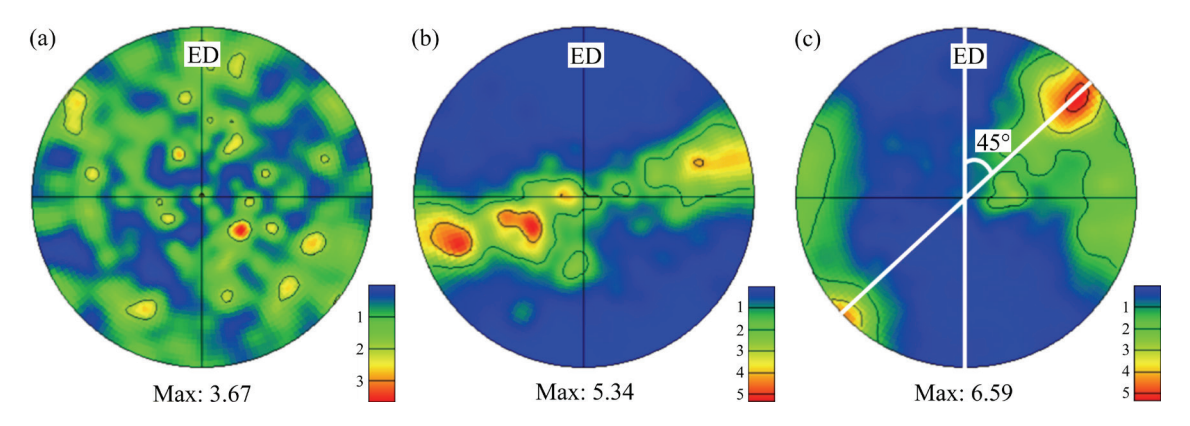


Fig. 14 (0001) pole figures of TAZ521 alloys with different processes: (a) Homogenization; (b) DE; (c) ES

density points are located randomly. The microtextures have differences from the macro-textures shown in Fig. 6, which is mainly caused by the test range. The EBSD test area is less than the area conducted by XRD. It can be seen from Fig. 14(b) that the DE-processed alloy exhibits a typical extruded texture with (0001) basal planes parallel to ED and the texture intensity value increases to 5.23. The basal slip, which is the easiest slip system, can hardly be activated at this orientation. Therefore, this orientation formed during the DE process can contribute to the improvement of strength, while the ductility is still suppressed due to the limited slip systems. The increase in the strain during extrusion may cause a decrease in the CRSS for dislocation slip [25]. After the ES process, the basal pole figure gradually exhibits a typical texture of ECAPed deformation, that is, the (0001) basal planes are 45° tilted to the ED, which indicates that the basal slip becomes available and is helpful for the improvement of ductility with activation of different slip systems [18]. It should be noted that the strength does not decrease due to the activity of basal slip; however, the maximum intensity of the (0001) pole figure shows a slight increase. On the other hand, the grains are further refined after the ES process, leading to higher strength.

4.3 Strengthening-plasticity mechanisms

4.3.1 Strengthening mechanism

For the extruded alloys, the increment of yield strength can be ascribed to grain refinement strengthening $(\Delta \sigma_g)$, precipitation strengthening $(\Delta \sigma_p)$, dislocation strengthening $(\Delta \sigma_d)$ and solution strengthening $(\Delta \sigma_{SS})$ effects. Thus, the total yield stress (σ_{YS}) could be estimated as follows [26]:

$$\sigma_{\rm YS} = \Delta \sigma_{\rm g} + \Delta \sigma_{\rm p} + \Delta \sigma_{\rm d} + \Delta \sigma_{\rm SS} \tag{2}$$

The solution strengthening contribution ($\Delta \sigma_{SS}$) can be presented as the equation [27]: $\Delta \sigma_{SS} = C \Delta X^{2/3}$, where C is the strengthening rate, and ΔX is the atomic fraction of solute. As the EDS results presented above, Sn and Al are mainly applied for the second phase particles, and thus the solid solution strengthening can be neglected.

The grain refinement strengthening could be calculated by the following Hall-Petch relationship [11]:

$$\Delta \sigma_{\rm g} = \sigma_0 + k d^{-1/2} \tag{3}$$

where σ_0 is the parameter determined in the polycrystalline material (taken as σ_0 =11 MPa) [27]; d is the average grain size; k is the material constant. In this work, the value of k is taken as 280 MPa· μ m^{-1/2} [28]. Consequently, contributions of grain refinement strengthening of the TAZ521 alloys after different processes are estimated to be 50.72, 138.80, and 178.33 MPa, respectively.

Based on Taylor formula, the strengthening contribution from residual dislocation can be calculated by [29]

$$\Delta \sigma_{\rm d} = M \alpha G b \sqrt{\rho_{\rm GND}} \tag{4}$$

where M is Taylor factor with value of 2.5 [30]; α is a constant with a value of 0.2, G is the shear modulus of Mg alloys (16.6 GPa). As the $\rho_{\rm GND}$ is already calculated in this work, the values of dislocation strengthening ($\Delta \sigma_{\rm d}$) of the ashomogenized, DE-processed, and ES-processed alloys are estimated to be 4.82, 17.00, and 18.01 MPa, respectively.

The high density of precipitates is dispersed in the α -Mg matrix, which inhibits the dislocation

motion and results in the strengthening effect. The YS increment $\Delta \tau_{\text{Orowan}}$ caused by precipitation strengthening can be estimated by the Orowan strengthening relationship as presented [31]:

$$\Delta\sigma_{p} = \frac{MGb}{2\pi\sqrt{1-\nu}\left(\frac{0.779}{\sqrt{f_{p}}} - 0.785\right)d_{p}} \ln\frac{0.785d_{p}}{b}$$
(5)

where ν is the Poisson ratio with value of 0.33. The volume fractions of precipitates (f_p) for the alloys processed in this work are 5.86%, 0.52%, and 0.59%, respectively. And d_p represents the average size of the spherical precipitates. According to the analysis obtained by SEM and TEM results, the values of d_p for alloys in this study are 770, 260.5, and 156.2 nm, respectively. Based on Eq. (5), the contributions of precipitation strengthening are estimated as 10.40, 6.39, and 10.51 MPa.

As illustrated in Fig. 15, The theoretically calculated results are close to the experimental results within the margin of error.

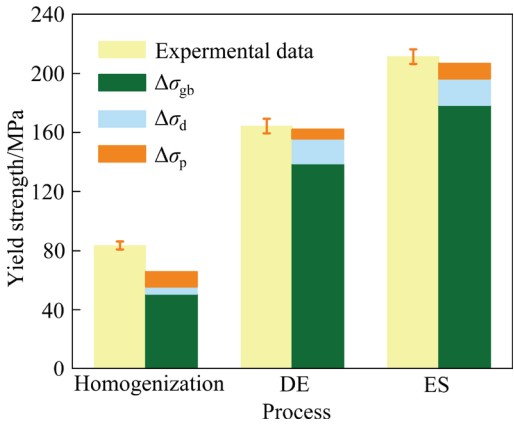


Fig. 15 Contributions of different strengthening mechanisms on yield stress of TAZ521 alloys with different processes

4.3.2 Plasticity mechanism

To investigate main deformation mechanism of the as-extruded alloy during the tensile deformation in this study, Fig. 16 reveals the Schmid factor (SF) maps and distribution for basal $\langle a \rangle$ slip, prismatic $\langle a \rangle$ slip, and pyramidal $\langle c+a \rangle$ slip of as-extruded alloys, respectively. The average SF values for three types of slip modes are >0.3. The SF value of basal $\langle a \rangle$ slip gradually increases to 0.36, while the SF values of the prismatic $\langle a \rangle$ slip and pyramidal $\langle c+a \rangle$ slip decrease slightly, which suggests that the CRSS decreases. Therefore, the basal slip can be easily

activated during the DE and ES processes. The changes for this phenomenon are probably attributed to the following reasons: firstly, the increase of fine DRXed grains makes the dislocation slip shorter and the finer and more homogeneous microstructure can decrease the CRSS difference between basal and non-basal slip systems [32]. Secondly, the stresses of grain boundary compatibility boost the cross-slip of basal dislocations to non-basal plans during deformation [33]. Thirdly, the dissolution of Mg₂Sn phases may contribute to reducing the CRSS anisotropy between basal and non-basal slip systems, which is beneficial to activating non-basal slip systems. Therefore, the ductility of the extruded alloys is improved according to the above reasons.

The ultimate tensile strength and elongation of magnesium alloys are summarized in Fig. 17. Noticeably, Mg–Sn binary alloys, Mg–Sn–Al based alloys, and Mg–Sn–Zn based alloys exhibit high strength, with an ultimate tensile strength of about 300 MPa. Moreover, the Mg–Sn–Zn based alloys show great ductility, with an elongation range from 20% to 30%. The Mg–Sn–Al–Zn based alloys possess higher UTS up to more than 350 MPa; however, they exhibit relatively poorer ductility. In comparison, the Mg–Sn–Al–Zn based alloys conducted by the ES process in this work show excellent strength and ductility.

The microstructure evolution during extrusion is illustrated in Fig. 18 for better understanding. The as-homogenized alloy shows an equiaxialgrained microstructure with some large secondary precipitates distributed along the grain boundaries and inside the grains. During hot extrusion, the initial coarse precipitates are broken and separated in the grains. Meanwhile, a large number of dislocations are accumulated along the grain boundaries and then LAGBs are formed, finally leading to the formation of HAGBs, which is known as CDRX. The newly generated DRXed grains are located along the grain boundaries, exhibiting a typical necklace structure. The dislocation regions with high density can lead to the migration of the GBs and sub-grain boundaries are formed. The accumulation of misorientation by the migration of LAGBs converts into HAGBs, turning the sub-grains into fine DRXed grains [19]. As the accumulative strain increases, the high storage energy drives the DRX nucleation through the PSN

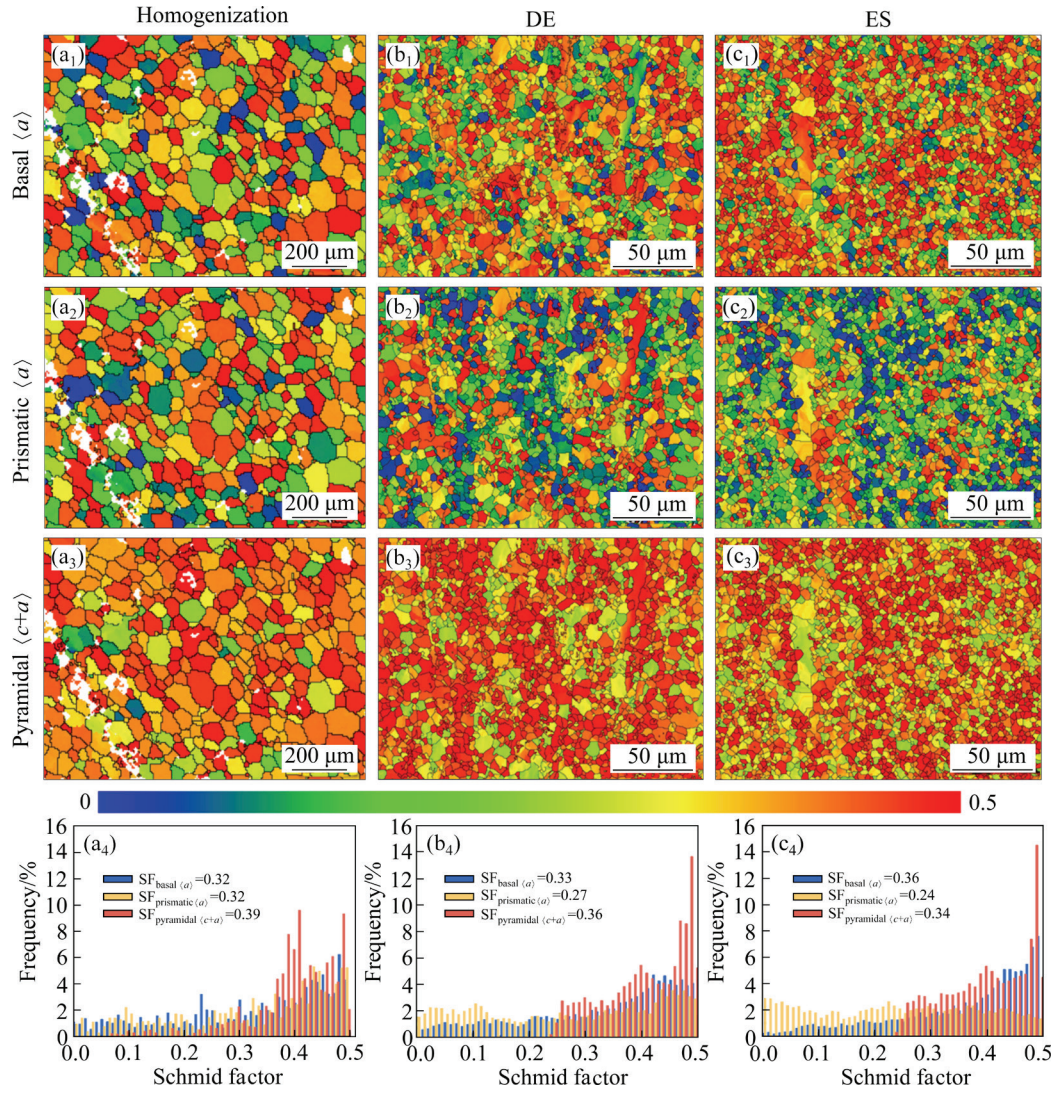


Fig. 16 Schmid factor maps for basal $\langle a \rangle$, prismatic $\langle a \rangle$, and pyramidal $\langle c+a \rangle$ slip systems of TAZ521 alloys and corresponding distributions of Schmid factors with different processes: (a_1-a_4) Homogenization; (b_1-b_4) DE; (c_1-c_4) ES

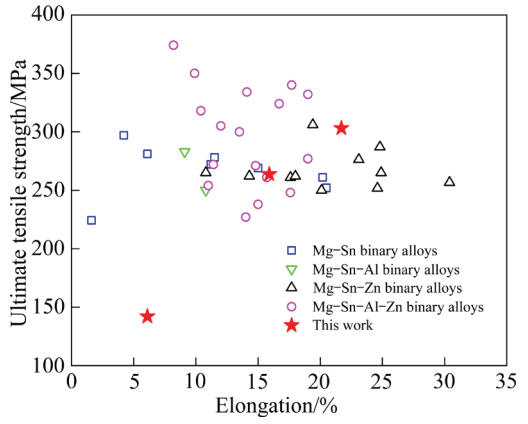


Fig. 17 Summary of ultimate tensile strength and elongation of extruded Mg-based alloys [8,13,14,34–50]

mechanism. At the end of the extrusion process, the microstructure is combined with both numerous DRXed grains and several unDRXed regions.

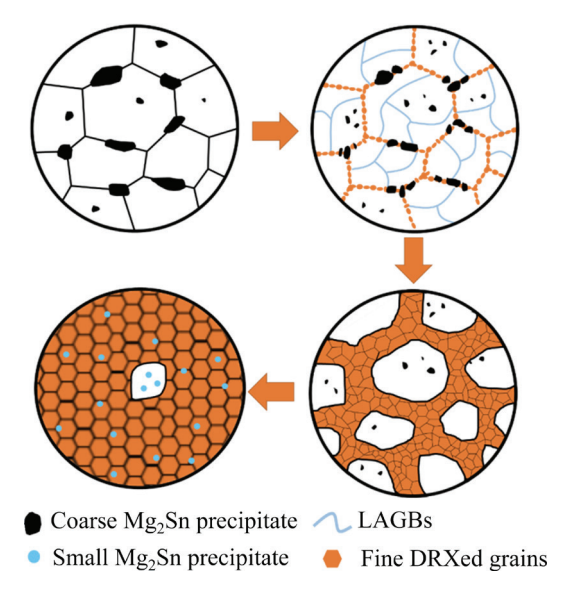


Fig. 18 Schematic illustration of microstructure evolution during extrusion

Moreover, the nano-scale precipitates contribute to hindering the growth of DRXed grains by the pinning effect. Therefore, the microstructure is finally refined through deformation.

5 Conclusions

- (1) After the hot extrusion, the grain size of the TAZ521 alloys was significantly decreased, especially the ES-processed alloys exhibited a more homogenous microstructure.
- (2) The Mg₂Sn phases were broken into nanoscale particles after extrusion and were equally located in the alloy. The Mg₂Sn phases contributed to the dynamic recrystallization behavior by hindering the movement of dislocations.
- (3) The mechanical properties of the TAZ521 alloys were significantly improved after the ES process. The YS and UTS of the ES-processed alloy reached 212 MPa and 303 MPa, respectively, which increased by 152.4% and 113.4% compared to those of the as-homogenized alloy. The enhancement of strength is owing to grain refinement strengthening and precipitate strengthening.
- (4) The elongation of the ES-processed alloy increased from 6.1% to 21.7%. The multiple slip modes including basal slips and non-basal slips contributed to the improvement of ductility, which indicates that the ES process is an effective method to enhance the strength without sacrificing the ductility.

CRediT authorship contribution statement

Feng-jian SHI: Conceptualization, Methodology, Project administration, Funding acquisition, Writing — Review & editing; Nan-ying PIAO: Methodology, Formal analysis, Investigation, Data curation, Visualization, Writing — Original draft, Writing — Review & editing; Ji-heng WANG: Methodology, Investigation, Validation; Hao-tian TAN: Methodology, Investigation, Validation, Writing — Review & editing; Yu-hang GUO: Methodology, Resources, Supervision; Fei YANG: Validation, Supervision; Shu-jin CHEN: Methodology, Supervision, Funding acquisition; Ze-xin WANG: Supervision, Funding acquisition.

Declaration of competing interest

The authors declare that they have no known competing financial interests or personal relationships that could have appeared to influence the work reported in this paper.

Acknowledgments

This research is supported by the Jiangsu Province Industry – University – Research Project, China (No. BY20221160), the Postgraduate Research and Practice Innovation Program of Jiangsu Province, China (No. KYCX22_3798), the National Natural Science Foundation of China (No. 52275339), the Key Research and Development Plan of the Ministry of Science and Technology, China (No. 2023YFE0200400), and the Science and Technology Project of Jiangsu Province, China (No. BZ2021053).

References

- [1] PENG Jin-hua, ZHANG Zhen, CHENG Huan-huan, CHEN Liang-yu, ZANG Qian-hao, LU Sheng, GUO Ting-ting, ZHOU Wei, WU Yu-cheng. Ambient extrusion induced working hardening and their effect on mechanical properties in AZ31 hot-extrusion bar [J]. Materials Science and Engineering A, 2022, 832: 142437.
- [2] WANG Xiao-xi, ZHANG Xiang, JING Xin-yu, YUAN Jun-chi, SONG Wei. Severe plastic deformation of commercially pure aluminum using novel equal channel angular expansion extrusion with spherical cavity [J]. Transactions of Nonferrous Metals Society of China, 2020, 30(10): 2613–2624.
- [3] WANG Li-fei, PAN Xiao-huan, ZHU Xing-xiao, XING Bin, ZHANG Hua, LU Li-wei, WANG Hong-xia, CHENG Wei-li, VEDANI M. Effect of two-step increased temperature thermal rolling on anisotropy and stretch formability of AZ31 magnesium alloy sheets [J]. Transactions of Nonferrous Metals Society of China, 2023, 33(4): 1066-1085.
- [4] SHI Feng-jian, PIAO Nan-ying, WANG Hao, WANG Ji-heng, ZANG Qian-hao, GUO Yu-hang, CHEN Cai, ZHANG Lu. Investigation of microstructure and mechanical properties of ZK60 magnesium alloy achieved by extrusion-shearing process [J]. Journal of Materials Research and Technology, 2023, 25: 799–811.
- [5] BETTLES C, GIBSON M. Current wrought magnesium alloys Strengths and weaknesses [J]. Journal of the Minerals, Metals & Materials Society, 2005, 57: 46–49.
- [6] WEI Shang-hai, ZHU Tian-ping, MICHAEL H, GAO Wei. Effects of Sn addition on the microstructure and mechanical properties of as-cast, rolled and annealed Mg-4Zn alloys [J]. Materials Science and Engineering A, 2013, 585: 139-148.
- [7] ELSAYED F R, SASAKI T T, MENDIS C L, OHKUBO T, HONO K. Compositional optimization of Mg-Sn-Al alloys for higher age hardening response [J]. Materials Science and Engineering A, 2013, 566: 22-29.
- [8] LUO Yu-xiao, CHEN Yu-an, RAN Lei, PANG Xu, PAN Fu-sheng. Effects of Zn/Al mass ratio on microstructure evolution and mechanical properties of Mg-Sn based alloys [J]. Materials Science and Engineering A, 2021, 815: 141307.
- [9] ZHANG Yang, CHEN Xiao-yang, LU Ya-lin, LI Xiao-ping. Microstructure and mechanical properties of as-extruded Mg-Sn-Zn-Ca alloy with different extrusion ratios [J]. Transactions of Nonferrous Metals Society of China, 2018,

- 28(11): 2190-2198.
- [10] WANG Cheng, ZHANG Hua-yuan, WANG Hui-yuan, LIU Guo-jun, JIANG Qi-chuan. Effects of doping atoms on the generalized stacking-fault energies of Mg alloys from first-principles calculations [J]. Scripta Materialia, 2013, 69(6): 445–448.
- [11] HALL E O. The deformation and ageing of mild steel. III: Discussion of results [J]. Proceedings of the Physical Society, 1951, 64: 747-753.
- [12] WANG Bo-ning, WANG Feng, WANG Zhi, ZHOU Le, LIU Zheng, MAO Ping-li. Microstructure and mechanical properties of Mg–Zn–Ca–Zr alloy fabricated by hot extrusion-shearing process [J]. Materials Science and Engineering A, 2020, 795: 139937.
- [13] PARK S H, YOU Bong-sun. Effect of homogenization temperature on the microstructure and mechanical properties of extruded Mg-7Sn-1Al-1Zn alloy [J]. Journal of Alloys and Compounds, 2015, 637: 332-338.
- [14] KIM Hyun-ji, JIN Sang-cheol, JUNG Jae-gil, PARK Sung-hyuk. Influence of undissolved second-phase particles on dynamic recrystallization behavior of Mg-7Sn-1Al-1Zn alloy during low- and high-temperature extrusions [J]. Journal of Materials Science & Technology, 2021, 71: 87-97.
- [15] GUO Yu-hang, HE Xuan-cheng, DAI Yi-bo, XIANG Hong-fu, ZANG Qian-hao, SHI Feng-jian, DONG Xuguang, ZHANG Zhen-ya. Microstructures and mechanical properties of Mg-5Li-4Sn-2Al-1Zn alloy after hot extrusion [J]. Materials Science and Engineering A, 2022, 860: 144329.
- [16] LIU Shuai-shuai, YANG Bang-peng, HUANG Guang-sheng, CHEN Xian-hua, TANG Ai-tao, JIANG Bin, ZHENG Kai-hong, PAN Fu-sheng. Effect of dual-heterogeneous microstructures on mechanical properties of AZ91 extruded sheet [J]. Transactions of Nonferrous Metals Society of China, 2023, 33(4): 1086–1097.
- [17] LI Jing-ren, XIE Dong-sheng, YU Han-song, LIU Ruo-lin, SHEN Yang-zi, ZHANG Xing-shuo, YANG Chang-lin, MA Li-feng, PAN Hu-cheng, QIN Gao-wu. Microstructure and mechanical property of multi-pass low-strain rolled Mg-Al-Zn-Mn alloy sheet [J]. Journal of Alloys and Compounds, 2020, 835: 155228.
- [18] CHEN Cai, HAN Dong-sheng, WANG Ming-chuan, XU Shun, CAI Ting, YANG Sen, SHI Feng-jian, BEAUSIR B, TOTH L S. High strength and high ductility of Mg-10Gd-3Y alloy achieved by a novel extrusion-shearing process [J]. Journal of Alloys and Compounds, 2023, 931: 167498.
- [19] XU Yu-zhao, LI Jing-yuan, QI Ming-fan, LIAO Lu-hai, GAO Zhi-jun. Enhanced mechanical properties of Mg-Zn-Y-Zr alloy by low-speed indirect extrusion [J]. Journal of Materials Research and Technology, 2020, 9(5): 9856–9867.
- [20] CHEN Hao, YANG Yan-mei, HU Fa-ping, LIU Xue-fei, KONG Fan-xiao, CUI Xiao-fei, XIE Wei-dong, WEI Guo-bing, YANG Yan, PENG Xiao-dong, HUANG Yuan-ding. Improvement of severe plastic deformation realized by several passes rotary swaging in the microstructure and properties of Mg-0.6Mn-0.5Al-0.5Zn-0.4Ca alloy [J]. Materials Science and Engineering A, 2023, 865: 144629.

- [21] ZHENG Jie, CHEN Zhe, YAN Zhao-ming, ZHANG Zhi-min, WANG Qiang, XUE Yong. Preparation of ultra-high strength Mg-Gd-Y-Zn-Zr alloy by pre-ageing treatment prior to extrusion [J]. Journal of Alloys and Compounds, 2022, 894: 162490.
- [22] PARK Chan-hee, OH Chang-seok, KIM Soo-ho. Dynamic recrystallization of the H- and O-tempered Mg AZ31 sheets at elevated temperatures [J]. Materials Science and Engineering A, 2012, 542: 127–139.
- [23] SITDIKOV O, KAIBYSHEV R. Dynamic recrystallization in pure magnesium [J]. Materials Transactions, 2001, 42: 1928–1937.
- [24] ROBSON J D, HENRY D T, DAVIS B. Particle effects on recrystallization in magnesium–manganese alloys: Particlestimulated nucleation [J]. Acta Materialia, 2009, 57: 2739–2747.
- [25] LEE DONG-HEE, LEE GYO-MYEONG, PARK SUNG-HYUK. Difference in extrusion temperature dependences of microstructure and mechanical properties between extruded AZ61 and AZ91 alloys [J]. Journal of Magnesium and Alloys, 2022, 11(5): 1683–1696.
- [26] JIANG Kun, ZHOU Ming-hang, WU Hao-xin, LIU Senzhong, WU Yu-juan, LIU Yong. Achieving the synergistic of strength and ductility in Mg-15Gd-1Zn-0.4Zr alloy with hierarchical structure [J]. Journal of Magnesium and Alloys, https://doi.org/10.1016/j.jma.2023.01.002.
- [27] HUTCHINSON C R, NIE J F, GORSSE S. Modeling the precipitation processes and strengthening mechanisms in a Mg-Al-(Zn) AZ91 alloy [J]. Metallurgical and Materials Transactions A, 2005, 36: 2093–2105.
- [28] LIU Xuan, ZHANG Zhi-qiang, HU Wen-yi, LE Qi-chi, BAO Lei, CUI Jian-zhong. Effects of extrusion speed on the microstructure and mechanical properties of Mg-9Gd-3Y-1.5Zn-0.8Zr alloy [J]. Journal of Materials Science & Technology, 2016, 32(4): 313-319.
- [29] DU Y Z, QIAO X G, ZHENG M Y, WU K, XU S W. The microstructure, texture and mechanical properties of extruded Mg–5.3Zn–0.2Ca–0.5Ce (wt.%) alloy [J]. Materials Science and Engineering A, 2015, 620: 164–171.
- [30] PAN Hu-cheng, KANG Rui, LI Jing-ren, XIE Hong-bo, ZENG Zhuo-ran, HUANG Qiu-yan, YANG Chang-lin, REN Yu-ping, QIN Gao-wu. Mechanistic investigation of a low-alloy Mg-Ca-based extrusion alloy with high strength ductility synergy [J]. Acta Materialia, 2020, 186: 278–290.
- [31] NIE J F. Effects of precipitate shape and orientation on dispersion strengthening in magnesium alloys [J]. Scripta Materialia, 2003, 48: 1009–1015.
- [32] SONG Jiang-feng, SHE Jia, CHEN Dao-lun, PAN Fu-sheng. Latest research advances on magnesium and magnesium alloys worldwide [J]. Journal of Magnesium and Alloys, 2020, 8: 1–41.
- [33] KOIKE J, KOBAYASHI T, MUKAI T, WATANABE H, SUZUKI M, MARUYAMA K, HIGASHI K. The activity of non-basal slip systems and dynamic recovery at room temperature in fine-grained AZ31B magnesium alloys [J]. Acta Materialia, 2003, 51: 2055–2065.
- [34] ZHAO Chao-yue, CHEN Xian-hua, PAN Fu-sheng, GAO Shang-yu, ZHAO Di, LIU Xiao-fang. Effect of Sn content on strain hardening behavior of as-extruded Mg-Sn alloys [J]. Materials Science and Engineering A, 2018, 713: 244-252.
- [35] EL MAHALLAWY N, AHMED DIAA A, AKDESIR M,

- PALKOWSKI H. Effect of Zn addition on the microstructure and mechanical properties of cast, rolled and extruded Mg-6Sn-xZn alloys [J]. Materials Science and Engineering A, 2017, 680: 47-53.
- [36] CHENG W L, PARK S S, YOU B S, KOO B H. Microstructure and mechanical properties of binary Mg-Sn alloys subjected to indirect extrusion [J]. Materials Science and Engineering A, 2010, 527: 4650-4653.
- [37] ZHAO Chao-yong, PAN Fu-sheng, ZHAO Shuang, PAN Hu-cheng, SONG Kai, TANG Ai-tao. Preparation and characterization of as-extruded Mg–Sn alloys for orthopedic applications [J]. Materials & Design, 2015, 70: 60–67.
- [38] JAYALAKSHMI S, SANKARANARAYANAN S, KOH S P X, GUPTA M. Effect of Ag and Cu trace additions on the microstructural evolution and mechanical properties of Mg-5Sn alloy [J]. Journal of Alloys and Compounds, 2013, 565: 56-65.
- [39] CHEN Yu-an, JIN Li, SONG Yu, LIU Hao, YE Rui-yu. Effect of Zn on microstructure and mechanical property of Mg-3Sn-1Al alloys [J]. Materials Science and Engineering A, 2014, 612: 96-101.
- [40] KIM SANG-HOON, PARK SUNG-HYUK. Underlying mechanisms of drastic reduction in yield asymmetry of extruded Mg-Sn-Zn alloy by Al addition [J]. Materials Science and Engineering A, 2018, 733: 285-290.
- [41] CHAI Yan-fu, JIANG Bin, SONG Jiang-feng, LIU Bo, HUANG Guang-sheng, ZHANG Ding-fei, PAN Fu-sheng. Effects of Zn and Ca addition on microstructure and mechanical properties of as-extruded Mg-1.0Sn alloy sheet [J]. Materials Science and Engineering A, 2019, 746: 82-93.
- [42] TANG W N, PARK S S, YOU B S. Effect of the Zn content on the microstructure and mechanical properties of indirect-extruded Mg–5Sn–xZn alloys [J]. Materials & Design, 2011, 32: 3537–3543.
- [43] CHENG Wei-li, PARK S S, TANG Wei-neng, YOU B S, KOO B H. Influence of rare earth on the microstructure and

- age hardening response of indirect-extruded Mg-5Sn-4Zn alloy [J]. Journal of Rare Earths, 2010, 28(5): 785-789.
- [44] KIM Beom-cheol, BAEK Soo-min, JEONG Hu-young, LEE Jung-gu, PARK Sung-soo. Grain refinement and reduced yield asymmetry of extruded Mg-5Sn-1Zn alloy by Al addition [J]. Journal of Alloys and Compounds, 2016, 660: 304-309
- [45] CHANG L L, TANG H, GUO J. Strengthening effect of nano and micro-sized precipitates in the hot-extruded Mg-5Sn-3Zn alloys with Ca addition [J]. Journal of Alloys and Compounds, 2017, 703: 552-559.
- [46] SHE Jia, PAN Fu-sheng, HU Huan-huan, PAN Hu-cheng, TANG Ai-tao, SONG Kai, YU Zheng-wen, LUO Su-qin. Microstructures and mechanical properties of as-extruded Mg-5Sn-1Zn-xAl (x=1, 3 and 5) alloys [J]. Progress in Natural Science: Materials International, 2015, 25(4): 267–275.
- [47] YAN Xu-dong, DING Wu-cheng, GUO Wen-wen, WU Jian-xun, SHU Hong, CHEN Yun-gui. The microstructure and mechanical properties of low-temperature and low-speed extruded Mg-3Sn-2Al-1Zn alloy [J]. Materials Science and Technology, 2020, 36(5): 575-583.
- [48] KIM Sang-hoon, PARK Sung-hyuk. Influence of Ce addition and homogenization temperature on microstructural evolution and mechanical properties of extruded Mg-Sn-Al-Zn alloy [J]. Materials Science and Engineering A, 2016, 676: 232–240.
- [49] KIM Sang-hoon, LEE Jong-un, KIM Ye-jin, JUNG Jae-gil, PARK Sung-hyuk. Controlling the microstructure and improving the tensile properties of extruded Mg-Sn-Zn alloy through Al addition [J]. Journal of Alloys and Compounds, 2018, 751: 1–11.
- [50] JUNG Jae-gil, PARK Sung-hyuk, YOU Bong-sun. Effect of aging prior to extrusion on the microstructure and mechanical properties of Mg-7Sn-1Al-1Zn alloy [J]. Journal of Alloys and Compounds, 2015, 627: 324-332.

通过不同热挤压方式制备具有较优强塑性组合的新型 Mg-5Sn-2Al-1Zn 合金

石凤健, 朴南瑛, 王冀恒, 谭昊天, 郭宇航, 杨 飞, 陈书锦, 芦 笙, 王泽鑫

江苏科技大学 材料科学与工程学院,镇江 212003

摘 要:制备新型 Mg-5Sn-2Al-1Zn(TAZ521)合金。为提高合金的强度与塑性,采用正挤压(DE)和挤压-剪切(ES)两种工艺对该合金进行变形处理。通过 XRD、SEM、TEM、EBSD 和拉伸试验等方法研究均匀态和挤压态合金的显微组织演变、织构演变及强化机制。结果表明,正挤压态合金的力学性能得到改善;然而,合金表现出由粗晶和细小动态再结晶(DRXed)晶粒组成的双峰组织。经过挤压-剪切变形后的合金组织变得更加均匀,并且实现更好的强韧性结合,变形后合金的屈服强度(YS)、极限抗拉强度(UTS)和伸长率(EL)分别达到 212 MPa、303 MPa 和21.7%。晶粒细化和 Mg2Sn 析出物的钉扎效应对强度的提高起到重要作用,此外,延展性的提高归因于基面纤维织构的弱化和非基面滑移系的激活。

关键词: Mg-Sn-Al-Zn 合金; 挤压-剪切; 晶粒细化; 力学性能; 织构演变